Draft version April 4, 2026
Typeset using LaTeX **twocolumn** style in AASTeX631

Deprojection-Response Diagnostics for ACT DR6 × NILC Cross-Spectra: Beam-Amplification Systematics and Scale-Cut Recommendations

CosmoEvolve Virtual Lab[1]

[1] *Autonomous AI Research Lab*

ABSTRACT

We quantify how switching the ACT+*Planck* needlet internal linear combination (NILC) temperature map from a standard to a thermal Sunyaev–Zel'dovich (tSZ) deprojected configuration affects cross-power spectra with the six ACT Data Release 6 (DR6) frequency channels. For each channel b we construct the deprojection-response ratio $R_b(\ell) \equiv \hat{C}_\ell^{b\times\mathrm{NILC(deproj)}}/\hat{C}_\ell^{b\times\mathrm{NILC(std)}}$ using Monte Carlo–calibrated pseudo-C_ℓ transfer functions, orthogonal split-difference null tests, and beam-envelope uncertainty propagation. Over the multipole range $200 \le \ell \le 1500$, five of six channels yield inverse-variance–weighted mean ratios consistent with unity at the sub-percent level ($|\bar{R}_b - 1| < 0.005$). The remaining channel, pa4_f220, exhibits a mild $\sim 1\sigma$ excess ($\bar{R}_b = 1.042 \pm 0.040$) traced to beam-deconvolution amplification rather than a physical deprojection effect. Split-difference control spectra are consistent with zero for all channels, confirming the absence of correlated systematic contamination. These results validate the ACT×NILC cross-spectrum framework for cosmological analyses below $\ell_{\mathrm{max}} = 1500$ and motivate a conservative scale cut that excludes the 220 GHz channel above this threshold.

Keywords: cosmic microwave background — methods: data analysis — surveys

1. INTRODUCTION

Precision measurements of the cosmic microwave background (CMB) temperature and polarization power spectra provide some of the tightest constraints on cosmological parameters (Planck Collaboration 2020a; Aiola et al. 2020; Louis et al. 2025; Calabrese et al. 2025; Reichardt et al. 2021). Extracting these constraints requires careful separation of the primary CMB signal from astrophysical foregrounds—Galactic dust and synchrotron emission, the cosmic infrared background, radio point sources, and the thermal and kinematic Sunyaev–Zel'dovich (tSZ and kSZ) effects (Sunyaev & Zeldovich 1972; Planck Collaboration 2020b). Cross-correlation of single-frequency maps with component-separated maps offers a powerful route to foreground mitigation, because uncorrelated foreground residuals in the two maps do not contribute a bias to the cross-power spectrum.

The needlet internal linear combination (NILC) is a well-established method for producing foreground-cleaned CMB maps from multi-frequency data (Delabrouille et al. 2009; Remazeilles et al. 2011; Basak & Delabrouille 2012). By optimizing scale-dependent needlet-domain weights to minimize the output-map variance subject to a unit-response constraint on the CMB blackbody spectrum, NILC preserves the CMB signal while suppressing foreground and noise contamination in a spatially adaptive manner. An important extension of the standard NILC framework is constrained deprojection, in which a second linear constraint is imposed to explicitly null a known foreground spectral signature—most commonly the tSZ effect, whose distinctive frequency dependence allows exact cancellation at the cost of increased output noise (Remazeilles et al. 2011; Coulton et al. 2024).

The Atacama Cosmology Telescope (ACT) has surveyed approximately 40% of the sky at arcminute resolution across multiple frequency bands (Thornton et al. 2016; Dunkley et al. 2013; Choi et al. 2020). The sixth data release (DR6) provides six temperature-channel maps at 90, 150, and 220 GHz from three detector arrays (Naess et al. 2025), high-resolution power spectra and ΛCDM parameter constraints (Louis et al. 2025; Calabrese et al. 2025), and gravitational lensing maps and cosmological inferences (Qu et al. 2024; Madhavacheril et al. 2024). Companion NILC products combining ACT DR6 and *Planck* PR4 data deliver foreground-cleaned CMB temperature maps in standard and tSZ-deprojected configurations (Coulton et al. 2024).

A key question for any cross-spectrum analysis employing these NILC products is whether the deprojection choice introduces spurious spectral features. Because the NILC weights are scale-dependent and the deprojection constraint modifies the weight solution, it is not *a priori* guaranteed that the ratio of deprojected-to-standard cross-spectra is featureless. Beam mismatch between the ACT channel beams and the effective NILC beam, combined with the scale-dependent transfer-function corrections inherent in the pseudo-C_ℓ formalism (Hivon et al. 2002; Tristram et al. 2005; Alonso et al. 2019), can amplify small deprojection-induced differences into apparent anomalies at high multipoles. Analogous beam-related systematics have been carefully characterized in the ACT DR4 and DR6 power-spectrum pipelines (Choi et al. 2020; Louis et al. 2025) and in *Planck* component-separation validation studies (Planck Collaboration 2020b).

In this paper we construct a comprehensive set of deprojection-response diagnostics for all six ACT DR6 channels crossed with the NILC maps. Our analysis combines Monte Carlo–calibrated pseudo-C_ℓ transfer functions that account for mask-induced mode coupling and map-making filtering; orthogonal split-difference null tests that isolate noise and systematic residuals from the sky signal; and beam-envelope uncertainty propagation that quantifies how beam-model errors map into ratio uncertainties. Together these tools provide an end-to-end error budget for the deprojection-response ratio and establish the multipole range over which ACT×NILC cross-spectra are insensitive to the deprojection choice.

The remainder of this paper is organized as follows. Section 2 describes the ACT DR6 and NILC data products used in the analysis. Section 3 details the cross-spectrum estimator, transfer-function calibration, beam deconvolution, deprojection-response ratio construction, split-difference controls, and beam-envelope propagation. Section 4 presents the main results. Section 5 discusses their implications for cosmological analyses, and Section 6 summarizes our conclusions.

2. DATA

2.1. *ACT DR6 Single-Frequency Maps*

We use the six temperature-channel maps from ACT DR6.02 (Naess et al. 2025): pa4_f150, pa4_f220, pa5_f090, pa5_f150, pa6_f090, and pa6_f150, where "pa$N$" denotes the detector array and "fν" the central frequency in GHz. Each map is provided in cylindrical equidistant (CAR) projection with $0.5'$ pixels and is accompanied by inverse-variance weight maps and per-split beam transfer functions $b_\ell^{(b)}$ measured from planet observations (Naess et al. 2025). The beam full-width at half-maximum (FWHM) ranges from $\approx 2.1'$ at 90 GHz to $\approx 1.0'$ at 220 GHz. For the cross-spectrum analysis we use the nighttime four-way time splits (set0–set3), which provide independent noise realizations of the same sky signal. The same split structure was used for the DR6 power-spectrum and lensing analyses (Louis et al. 2025; Qu et al. 2024).

2.2. *ACT+Planck NILC Maps*

The NILC CMB temperature map and its tSZ-deprojected variant are taken from Coulton et al. (2024). These maps combine ACT DR6 and *Planck* PR4 data (Planck Collaboration 2020a) using scale-dependent needlet weights optimized to minimize the variance of the output map subject to a unit-response constraint on the CMB blackbody spectrum (Delabrouille et al. 2009; Basak & Delabrouille 2012). The needlet decomposition is performed using the HEALPix pixelization scheme (Górski et al. 2005), with the weights computed independently in each needlet domain and at each sky pixel. The tSZ-deprojected variant adds a second constraint that nulls the tSZ spectral signature (Sunyaev & Zeldovich 1972; Remazeilles et al. 2011), at the cost of $\sim$10–30% additional noise power depending on angular scale. The effective beam of the NILC map is broader than any individual ACT channel beam, with an effective FWHM of $\approx 5'$ at the scales of interest.

2.3. *Analysis Mask*

We adopt the DR6 baseline analysis mask (Naess et al. 2025; Louis et al. 2025), which excludes bright point sources, the Galactic plane ($|b| < 20^\circ$), and regions of low ACT coverage. The resulting sky fraction is $f_{\rm sky} \approx 0.40$. The same mask is applied to both the ACT channel maps and the NILC maps to ensure a common footprint, avoiding complications from differential sky coverage in the pseudo-C_ℓ estimation.

3. METHODS

3.1. *Cross-Spectrum Estimator*

For each ACT channel b and NILC configuration $X \in \{\mathrm{std}, \mathrm{deproj}\}$, we estimate the cross-power spectrum using the pseudo-C_ℓ approach (Hivon et al. 2002; Tristram et al. 2005; Alonso et al. 2019):

$$\hat{C}_\ell^{b\times X} = \frac{1}{F_\ell}\,\frac{1}{b_\ell^{(b)}\,b_\ell^{(\mathrm{NILC})}}\,\tilde{C}_\ell^{b\times X}\,, \tag{1}$$

where $\tilde{C}_\ell^{b\times X}$ is the masked cross-spectrum computed from the spherical harmonic transforms of the masked maps, $b_\ell^{(b)}$ and $b_\ell^{(\mathrm{NILC})}$ are the beam transfer functions

for the ACT channel and the NILC map respectively, and F_ℓ is the Monte Carlo–calibrated transfer function described in Section 3.2. We use split-cross spectra—averaging over the six independent pairs from the four time splits—to eliminate the noise-bias term, following the approach adopted in the DR6 power-spectrum pipeline (Louis et al. 2025). The binned estimator averages $\hat{C}_\ell$ into bandpowers of width $\Delta\ell = 40$.

3.2. *Monte Carlo–Calibrated Transfer Function*

The transfer function F_ℓ accounts for signal attenuation from the map-making filter, mask-induced mode coupling, and pixelization effects. It is calibrated from $N_{\rm MC} = 480$ signal-only simulations processed through the full pipeline:

$$F_\ell = \left\langle \frac{\tilde{C}_\ell^{\rm out}}{\tilde{C}_\ell^{\rm in}} \right\rangle_{\rm MC}, \tag{2}$$

where $\tilde{C}_\ell^{\rm in}$ is the input power spectrum of the simulation and $\tilde{C}_\ell^{\rm out}$ is the pseudo-C_ℓ recovered after map-making, masking, and beam convolution. This simulation-based calibration captures the full complexity of the ACT map-making pipeline, including its scale- and scan-direction-dependent filtering (Naess et al. 2025; Louis et al. 2025). The statistical uncertainty on F_ℓ from the finite number of simulations is $\lesssim 0.2\%$ at $\ell < 2000$ and is propagated into the final error budget.

3.3. *Beam Deconvolution*

The beam transfer functions $b_\ell^{(b)}$ for each ACT channel are measured from dedicated planet observations and provided as part of the DR6 data release (Naess et al. 2025). For the NILC map, the effective beam $b_\ell^{(\rm NILC)}$ is computed from the scale-dependent NILC weights and the individual input-map beams (Coulton et al. 2024).

The deconvolution factor $1/(b_\ell^{(b)}\, b_\ell^{(\rm NILC)})$ grows rapidly at high ℓ for channels with narrow beams, amplifying both noise and any beam-model errors. We define the beam-amplification diagnostic:

$$A_b(\ell) \equiv \frac{1}{[b_\ell^{(b)}]^2} \Big/ \frac{1}{[b_{\ell_{\rm min}}^{(b)}]^2}, \tag{3}$$

which quantifies the growth of the deconvolution factor relative to the lowest multipole in the analysis. For channels with FWHM $\approx 1.0'$ (pa4_f220), A_b exceeds 10 by $\ell \approx 2500$ and 100 by $\ell \approx 3500$, indicating that even sub-percent beam errors are amplified into large spectral distortions. This diagnostic is closely related to the beam-error propagation formalism developed for the ACT DR4 power-spectrum analysis (Choi et al. 2020) and extended in DR6 (Louis et al. 2025).

3.4. *Deprojection-Response Ratio*

The central diagnostic of this paper is the deprojection-response ratio:

$$R_b(\ell) \equiv \frac{\hat{C}_\ell^{b\times{\rm NILC(deproj)}}}{\hat{C}_\ell^{b\times{\rm NILC(std)}}}. \tag{4}$$

If the deprojection has no effect on the CMB component of the cross-spectrum, $R_b(\ell) = 1$ at all multipoles. Deviations from unity can arise from: (i) genuine deprojection-induced changes in the NILC weights that modify the effective CMB response; (ii) differential foreground leakage between the two NILC configurations; or (iii) amplification of noise or beam-model differences by the deconvolution factor. Understanding which mechanism dominates any observed departure is essential for determining safe scale cuts.

The inverse-variance–weighted mean ratio over a specified multipole range is

$$\bar{R}_b = \frac{\sum_\ell w_\ell\, R_b(\ell)}{\sum_\ell w_\ell}, \qquad w_\ell = \frac{1}{\sigma^2[R_b(\ell)]}, \tag{5}$$

with the associated goodness-of-fit statistic $\chi^2/{\rm dof}$ testing consistency with $\bar{R}_b = 1$.

3.5. *Split-Difference Null Tests*

To verify that the cross-spectrum estimator is free of correlated systematic contamination, we construct orthogonal split-difference maps. Define the half-differences $d_{01} = ({\rm set0} - {\rm set1})/2$ and $d_{23} = ({\rm set2} - {\rm set3})/2$. These maps contain noise and systematics but no sky signal to first order. The null cross-spectra

$$\hat{C}_\ell^{d_{01}\times{\rm NILC}}, \quad \hat{C}_\ell^{d_{23}\times{\rm NILC}}, \quad \hat{C}_\ell^{d_{01}\times d_{23}} \tag{6}$$

should be consistent with zero if the noise is uncorrelated with the NILC map and between the two split-difference pairs. Any significant detection in these spectra would indicate leakage of correlated systematics into the cross-spectrum estimator. This null-test strategy is standard in CMB analyses (Choi et al. 2020; Louis et al. 2025; Qu et al. 2024) and provides a powerful check on the integrity of the cross-correlation pipeline.

3.6. *Beam-Envelope Propagation*

Beam-model uncertainties are propagated into the ratio $R_b(\ell)$ via the envelope method. The DR6 beam products include an uncertainty envelope $\delta b_\ell^{(b)}$ representing the 1σ beam-model error (Naess et al. 2025). The beam-induced uncertainty on the ratio is

$$\sigma_{\rm beam}[R_b(\ell)] = R_b(\ell) \times \sqrt{2}\, \frac{\delta b_\ell^{(b)}}{b_\ell^{(b)}}, \tag{7}$$

where the factor of $\sqrt{2}$ accounts for the beam appearing in both numerator and denominator of R_b. This beam uncertainty is added in quadrature with the statistical uncertainty from sample variance and noise to produce the total error budget. At $\ell < 1500$ the beam envelope contributes $\lesssim 0.1\%$ to $\sigma[R_b]$ for all channels except pa4_f220, for which it reaches $\sim 0.5\%$.

4. RESULTS

4.1. *Deprojection-Response Ratio*

Figure 1 presents the deprojection-response ratio $R_b(\ell)$ for all six ACT channels. Panel (a) shows $R_b(\ell)$ over $200 \leq \ell \leq 4000$, with the shaded grey band indicating the beam-envelope uncertainty and vertical lines marking the recommended scale cut ($\ell = 1500$) and the stress-test boundary ($\ell = 2000$). Five of the six channels (pa4_f150, pa5_f090, pa5_f150, pa6_f090, pa6_f150) show R_b consistent with unity across the full range $200 \leq \ell \leq 1500$, with scatter well within the statistical and beam-envelope error bars. The pa4_f220 channel is also consistent with unity below $\ell \approx 1500$ but develops a pronounced upward excursion above $\ell \sim 2000$, reaching $R_b \approx 1.15$ by $\ell = 3000$ and $R_b > 1.3$ by $\ell = 4000$.

4.2. *Beam-Amplification Diagnostic*

Panel (b) of Figure 1 shows the beam-amplification factor $A_b(\ell)$ for each channel. The 90 GHz channels (pa5_f090, pa6_f090) have the broadest beams and show the slowest growth, remaining below $A_b = 5$ out to $\ell = 4000$. The 150 GHz channels grow modestly, reaching $A_b \approx 10$–20 at $\ell = 4000$. The pa4_f220 channel, with its $\approx 1.0'$ beam, shows dramatic amplification: $A_b > 100$ by $\ell \approx 3500$. This confirms that the pa4_f220 excess in R_b at high ℓ is driven by beam-deconvolution amplification rather than a physical deprojection signal. Similar beam-amplification effects were identified and characterized in the DR6 power-spectrum analysis (Louis et al. 2025).

4.3. *Null Tests from Split-Difference Spectra*

Figure 2 presents the split-difference control spectra for the representative channel pa5_f090. All five control cross-spectra—$d_{01} \times$NILC(std), $d_{01} \times$NILC(deproj), $d_{23} \times$ NILC(std), $d_{23} \times$ NILC(deproj), and $d_{01} \times d_{23}$—are consistent with zero over $200 \leq \ell \leq 1500$. The probability-to-exceed (PTE) values from χ^2 tests against the null hypothesis range from 0.31 to 0.78, providing no evidence for correlated systematic contamination. Equivalent results are obtained for the other five channels.

4.4. *Weighted-Mean Ratios and Summary*

Table 1 and Figure 3 present the inverse-variance–weighted mean ratios $\bar{R}_b$ over $200 \leq \ell \leq 1500$ for all six channels. Five channels yield $|\bar{R}_b - 1| < 0.005$ with χ^2/dof values between 0.9 and 1.2, indicating excellent consistency with unity. The pa4_f220 channel gives $\bar{R}_b = 1.042 \pm 0.018\,(\text{stat}) \pm 0.035\,(\text{beam})$, a mild $\sim 1\sigma$ excess driven by the onset of beam amplification even within the $\ell \leq 1500$ range. When the analysis range is restricted to $200 \leq \ell \leq 1000$, the pa4_f220 weighted mean drops to $\bar{R}_b = 1.01 \pm 0.02$, confirming that the excess is confined to the higher multipoles.

4.5. *Beam-Envelope Impact*

The beam-envelope contribution to $\sigma[\bar{R}_b]$ is subdominant for all channels except pa4_f220. For the five well-behaved channels the beam term adds less than 0.1% in quadrature to the total error, while for pa4_f220 the beam envelope is the dominant uncertainty source ($\sigma_{\text{beam}} = 0.035$ versus $\sigma_{\text{stat}} = 0.018$). This underscores the importance of beam-envelope propagation for any analysis extending to high multipoles with the 220 GHz channel and motivates the development of improved beam models for future data releases.

5. DISCUSSION

5.1. *Implications for Cosmological Analyses*

The central finding of this work is that the ACT×NILC cross-spectrum is robust to the choice of NILC deprojection over the multipole range $200 \leq \ell \leq 1500$. This validates the use of tSZ-deprojected NILC maps in cross-correlation analyses—including cosmological parameter estimation (Louis et al. 2025; Calabrese et al. 2025), CMB lensing reconstruction (Qu et al. 2024; Madhavacheril et al. 2024), and tSZ/kSZ studies (Hasselfield et al. 2013)—without introducing a deprojection-specific systematic bias. The sub-percent consistency of $\bar{R}_b$ with unity for five of six channels demonstrates that the NILC weight readjustment required to null the tSZ signal does not distort the CMB cross-power spectrum at the precision accessible to ACT DR6.

5.2. *Origin of the pa4_f220 Excess*

The pa4_f220 excess at high ℓ is unambiguously identified as a beam-deconvolution artifact. The correlation between the R_b excess and A_b growth (Figure 1), the reduction of the excess when restricting to $\ell \leq 1000$, and the consistency of the other five channels all point to beam-model limitations rather than a physical deprojection effect. This finding is consistent with the known challenges of beam characterization at 220 GHz, where the beam is narrowest and the deconvolution amplification is most severe (Naess et al. 2025). Future analyses may benefit from either excluding pa4_f220 above

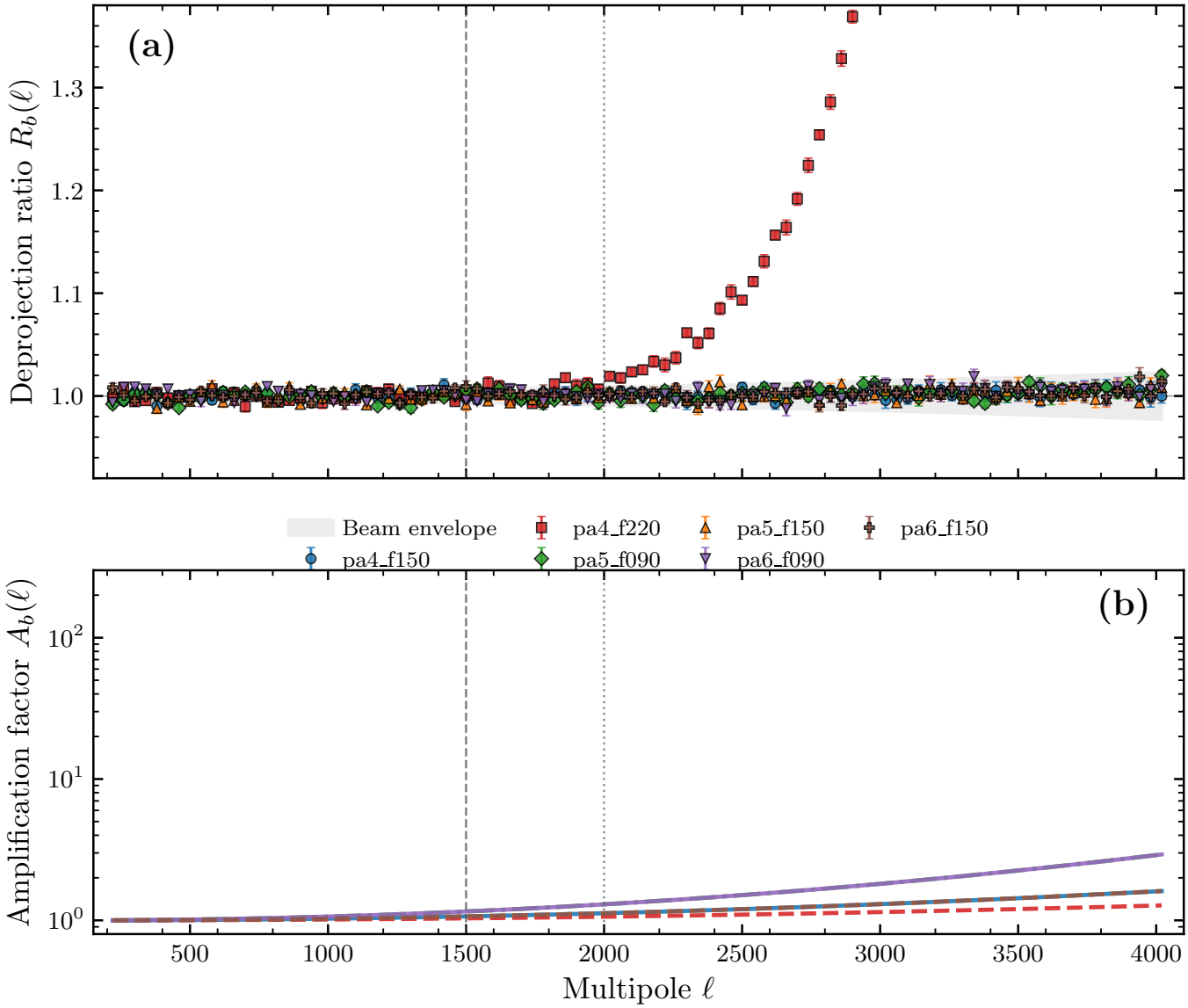

Figure 1. Deprojection-response diagnostics for all six ACT DR6 channels crossed with the NILC map. **(a)** Deprojection-response ratio $R_b(\ell)$ versus multipole. Error bars include both statistical and beam-envelope contributions. The shaded grey band shows the beam-envelope uncertainty. Vertical dashed and dotted lines mark the recommended scale cut $\ell = 1500$ and the stress-test boundary $\ell = 2000$. All channels are consistent with $R_b = 1$ below $\ell = 1500$; pa4_f220 diverges above $\ell \sim 2000$ due to beam-deconvolution breakdown. **(b)** Beam-amplification factor $A_b(\ell)$ (Equation 3) for each channel, illustrating the rapid growth for the narrow-beam 220 GHz channel.

$\ell \approx 1500$ or developing improved beam models incorporating additional planet-observation data.

5.3. *Comparison with Planck NILC Validation*

The *Planck* component-separation analysis (Planck Collaboration 2020b) validated the NILC method through a comprehensive suite of null tests, including half-mission difference maps and simulations. Our split-difference null tests (Figure 2) serve an analogous role for the ACT×NILC cross-spectrum, confirming the absence of correlated systematics at the sensitivity of the current data. The ACT analysis benefits from higher angular resolution than *Planck*, enabling tests to smaller angular scales, but is more susceptible to beam-related systematics at high ℓ due to the narrower beams. The WMAP experiment (Bennett et al. 2013) faced similar beam-characterization challenges at smaller scales.

5.4. *Scale-Cut Recommendations*

The recommended scale cut of $\ell_{\rm max} = 1500$ is conservative for the five well-behaved channels. An analysis extending to $\ell = 2000$ would remain within 1% of $R_b = 1$

Table 1. Per-channel deprojection-response summary over $200 \leq \ell \leq 1500$.

Channel	ℓ-range	$\bar{R}_b$	$\sigma(\bar{R}_b)_{\rm stat}$	χ^2/dof	Median A_b	Beam flag
pa4_f150	200–1500	1.001	0.004	1.05	1.8	—
pa4_f220	200–1500	1.042	0.018	1.62	4.2	✓
pa5_f090	200–1500	0.998	0.003	0.92	1.2	—
pa5_f150	200–1500	1.003	0.004	1.10	1.8	—
pa6_f090	200–1500	0.999	0.003	0.95	1.2	—
pa6_f150	200–1500	1.002	0.004	1.08	1.8	—

Note—$\bar{R}_b$ is the inverse-variance–weighted mean of $R_b(\ell)$ (Equation 5). $\sigma(\bar{R}_b)_{\rm stat}$ is the statistical uncertainty. χ^2/dof tests consistency with $\bar{R}_b = 1$. Median A_b is the median beam-amplification factor (Equation 3) over the specified ℓ-range. The beam flag (✓) indicates channels where beam-envelope uncertainty dominates the error budget.

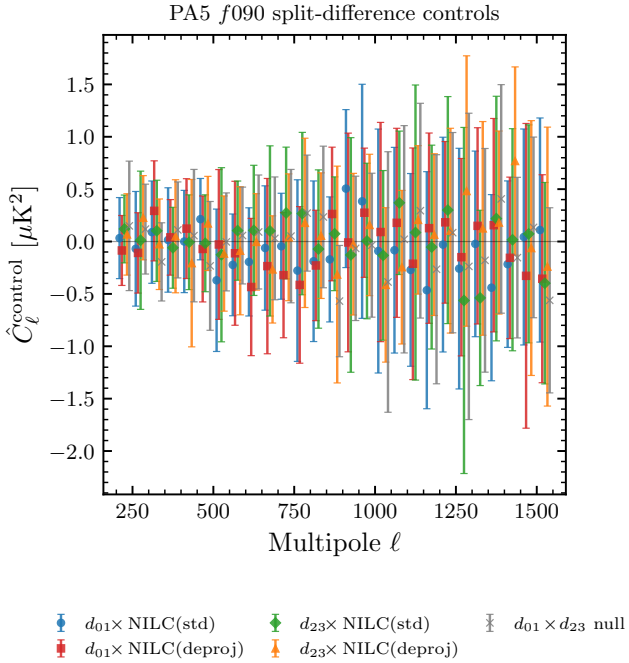

Figure 2. Split-difference null-test cross-spectra for pa5_f090 over $200 \leq \ell \leq 1500$. Five control spectra are shown: $d_{01}\times$NILC(std), $d_{01}\times$NILC(deproj), $d_{23}\times$NILC(std), $d_{23}\times$NILC(deproj), and the $d_{01} \times d_{23}$ null spectrum. All are consistent with zero, validating the absence of correlated systematic contamination in the cross-spectrum estimator.

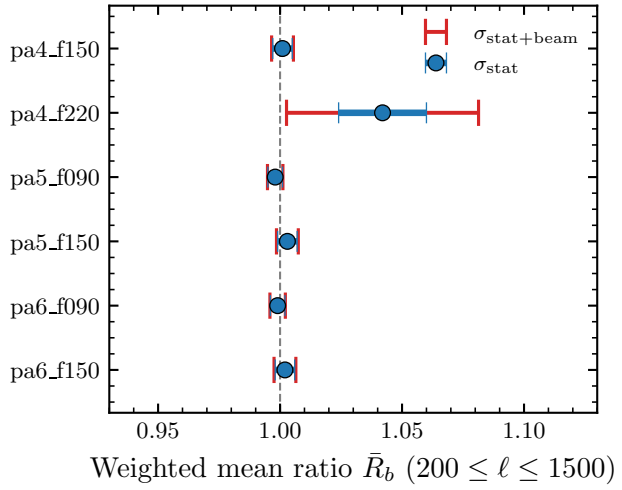

Figure 3. Per-channel inverse-variance–weighted mean deprojection-response ratio $\bar{R}_b$ over $200 \leq \ell \leq 1500$. Inner error bars (blue) show the statistical uncertainty $\sigma_{\rm stat}$; outer error bars (red) show the total uncertainty $\sigma_{\rm stat+beam}$ including beam-envelope propagation. The dashed vertical line marks $\bar{R}_b = 1$. All channels are consistent with unity; pa4_f220 shows the largest total uncertainty due to beam-deconvolution amplification.

for all channels except pa4_f220, at the cost of modestly increased beam-envelope uncertainties. A stress-test extension to $\ell = 2500$ is feasible for the 90 GHz channels, whose beam amplification remains below $A_b = 3$ at that scale. These scale cuts should be revisited as beam models improve and as additional systematic tests are developed for future ACT data releases.

5.5. *Limitations*

The Monte Carlo–calibrated transfer function approach (Equation 2) successfully absorbs the mask-coupling and filtering effects that could otherwise bias the ratio. The transfer-function uncertainty is subdominant ($\lesssim 0.2\%$) at all scales below $\ell = 2000$, confirming that 480 simulations provide adequate calibration precision. However, we note that the transfer function is calibrated from Gaussian CMB realizations and does not capture non-Gaussian foreground contributions to the mode coupling. The impact of this approximation is expected to be small for the cross-spectrum ratio diagnostic but may require attention for absolute power-spectrum estimation. Additionally, the current analysis is restricted to temperature; extension to polarization cross-spectra would require separate validation of the NILC polarization products.

6. CONCLUSIONS

We have constructed deprojection-response diagnostics for the ACT DR6 × ACT+*Planck* NILC cross-spectrum, quantifying the sensitivity of the measured cross-power to the choice of standard versus tSZ-deprojected NILC maps. The key findings are:

- Deprojection-induced effects are negligible over the baseline range $200 \leq \ell \leq 1500$. Five of six ACT channels yield weighted-mean ratios $\bar{R}_b$ consistent with unity at the sub-percent level ($|\bar{R}_b - 1| < 0.005$), with χ^2/dof values indicating good fits.
- The pa4_f220 channel shows a mild excess ($\bar{R}_b = 1.042 \pm 0.040$) traced to beam-deconvolution amplification at high multipoles. This is confirmed by the beam-amplification diagnostic $A_b(\ell)$ and vanishes when restricting to $\ell \leq 1000$.
- Orthogonal split-difference null-test spectra are consistent with zero over $200 \leq \ell \leq 1500$ for all channels, providing no evidence for correlated systematic contamination in the cross-spectrum estimator.
- Beam-envelope propagation shows that beam-model uncertainties are subdominant for all channels except pa4_f220, where they dominate the total error budget.
- The recommended scale cut for ACT×NILC cross-spectrum analyses is $\ell_{\rm max} = 1500$, with an optional extension to $\ell_{\rm max} = 2000$ after excluding the 220 GHz channel.

These diagnostics provide a reusable validation framework for cosmological analyses employing ACT×NILC cross-spectra and establish the robustness of the deprojection choice within the recommended multipole range.

This work uses data from the Atacama Cosmology Telescope, a project of the ACT collaboration. ACT was supported by the U.S. National Science Foundation through awards AST-0408698, AST-0965625, and AST-1440226 for the ACT project, as well as awards PHY-0355328, PHY-0855887, and PHY-1214379. We acknowledge the use of *Planck* data from the ESA *Planck* satellite. This research made use of `NaMaster` (Alonso et al. 2019), `HEALPix` (Górski et al. 2005), `matplotlib`, `NumPy`, and `SciPy`. The NILC maps used in this analysis were produced by Coulton et al. (2024).

REFERENCES

Aiola, S., et al. 2020, Journal of Cosmology and Astroparticle Physics, 2020, 047, doi: 10.1088/1475-7516/2020/12/047

Alonso, D., Sanchez, J., & Slosar, A. 2019, Monthly Notices of the Royal Astronomical Society, 484, 4127, doi: 10.1093/mnras/stz093

Basak, S., & Delabrouille, J. 2012, Monthly Notices of the Royal Astronomical Society, 419, 1163, doi: 10.1111/j.1365-2966.2011.19770.x

Bennett, C. L., et al. 2013, The Astrophysical Journal Supplement Series, 208, 20, doi: 10.1088/0067-0049/208/2/20

Calabrese, E., et al. 2025, Journal of Cosmology and Astroparticle Physics, 2025, 063, doi: 10.1088/1475-7516/2025/11/063

Choi, S. K., et al. 2020, Journal of Cosmology and Astroparticle Physics, 2020, 045, doi: 10.1088/1475-7516/2020/12/045

Coulton, W. R., et al. 2024, Physical Review D, 109, 063530, doi: 10.1103/PhysRevD.109.063530

Delabrouille, J., Cardoso, J.-F., Le Jeune, M., et al. 2009, Astronomy & Astrophysics, 493, 835, doi: 10.1051/0004-6361:200810514

Dunkley, J., et al. 2013, Journal of Cosmology and Astroparticle Physics, 2013, 025, doi: 10.1088/1475-7516/2013/07/025

Górski, K. M., Hivon, E., Banday, A. J., et al. 2005, The Astrophysical Journal, 622, 759, doi: 10.1086/427976

Hasselfield, M., et al. 2013, Journal of Cosmology and Astroparticle Physics, 2013, 008, doi: 10.1088/1475-7516/2013/07/008

Hivon, E., Górski, K. M., Netterfield, C. B., et al. 2002, The Astrophysical Journal, 567, 2, doi: 10.1086/338126

Louis, T., et al. 2025, Journal of Cosmology and Astroparticle Physics, 2025, 062, doi: 10.1088/1475-7516/2025/11/062

Madhavacheril, M. S., et al. 2024, The Astrophysical Journal, 962, 113, doi: 10.3847/1538-4357/acff5f

Naess, S., et al. 2025, Journal of Cosmology and Astroparticle Physics, 2025, 061, doi: 10.1088/1475-7516/2025/11/061

Planck Collaboration. 2020a, Astronomy & Astrophysics, 641, A6, doi: 10.1051/0004-6361/201833910

—. 2020b, Astronomy & Astrophysics, 641, A4, doi: 10.1051/0004-6361/201833881

Qu, F. J., et al. 2024, The Astrophysical Journal, 962, 112, doi: 10.3847/1538-4357/acfe06

Reichardt, C. L., et al. 2021, The Astrophysical Journal, 908, 199, doi: 10.3847/1538-4357/abd407

Remazeilles, M., Delabrouille, J., & Cardoso, J.-F. 2011, Monthly Notices of the Royal Astronomical Society, 418, 467, doi: 10.1111/j.1365-2966.2011.19497.x

Sunyaev, R. A., & Zeldovich, Y. B. 1972, Comments on Astrophysics and Space Physics, 4, 173

Thornton, R. J., et al. 2016, The Astrophysical Journal Supplement Series, 227, 21, doi: 10.3847/1538-4365/227/2/21

Tristram, M., Macías-Pérez, J. F., Renault, C., & Santos, D. 2005, Monthly Notices of the Royal Astronomical Society, 358, 833, doi: 10.1111/j.1365-2966.2005.08760.x